

Ozone oxidation methods for aluminum oxide formation

Gupta, S.; Hannah, S.; Watson, Colin; Šutta, P. ; Pedersen, R.H. ; Gleskova, H.

Organic Electronics

DOI:

[10.1016/j.orgel.2015.03.007](https://doi.org/10.1016/j.orgel.2015.03.007)

Published: 01/06/2015

Publisher's PDF, also known as Version of record

[Cyswllt i'r cyhoeddiad / Link to publication](#)

Dyfyniad o'r fersiwn a gyhoeddwyd / Citation for published version (APA):

Gupta, S., Hannah, S., Watson, C., Šutta, P., Pedersen, R. H., & Gleskova, H. (2015). Ozone oxidation methods for aluminum oxide formation: Application to low-voltage organic transistors. *Organic Electronics*, 21, 132-137. <https://doi.org/10.1016/j.orgel.2015.03.007>

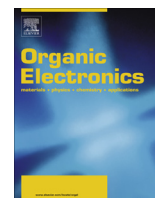
Hawliau Cyffredinol / General rights

Copyright and moral rights for the publications made accessible in the public portal are retained by the authors and/or other copyright owners and it is a condition of accessing publications that users recognise and abide by the legal requirements associated with these rights.

- Users may download and print one copy of any publication from the public portal for the purpose of private study or research.
- You may not further distribute the material or use it for any profit-making activity or commercial gain
- You may freely distribute the URL identifying the publication in the public portal ?

Take down policy

If you believe that this document breaches copyright please contact us providing details, and we will remove access to the work immediately and investigate your claim.



Ozone oxidation methods for aluminum oxide formation: Application to low-voltage organic transistors



S. Gupta^{a,1}, S. Hannah^a, C.P. Watson^b, P. Šutta^c, R.H. Pedersen^d, N. Gadegaard^d, H. Gleskova^{a,*}

^a Department of Electronic and Electrical Engineering, University of Strathclyde, Glasgow G1 1XW, United Kingdom

^b School of Electronic Engineering, Bangor University, Dean Street, Bangor, Gwynedd LL57 1UT, United Kingdom

^c New Technologies Research Centre, University of West Bohemia, Univerzitní 8, 306 14 Pilsen, Czech Republic

^d School of Engineering, University of Glasgow, Glasgow G12 8QQ, United Kingdom

ARTICLE INFO

Article history:

Received 27 January 2015

Received in revised form 26 February 2015

Accepted 5 March 2015

Available online 9 March 2015

Keywords:

Aluminum oxide

Ozone oxidation

FTIR

XPS

Organic thin-film transistors

ABSTRACT

Four atmospheric pressure ozone oxidation methods were used to produce ultra-thin layers of aluminum oxide for organic thin-film transistors. They are UV/ozone oxidation in ambient (UV-AA) and dry (UV-DA) air, UV/ozone oxidation combined with high-voltage discharge-generated ozone in dry air (UV+O₃-DA), and discharge-generated ozone in dry air (O₃-DA). The lack of the high-energy UV photons during the O₃-DA oxidation led to low relative permittivity and high leakage current density of the AlO_x layer that rendered this method unsuitable for transistor dielectrics. Although this oxidation method led to the incorporation of oxygen into the film, the FTIR confirmed an increased concentration of the subsurface oxygen while the XPS showed the highest portion of the unoxidized Al among all four methods. The remaining three oxidation methods produced AlO_x films with thicknesses in excess of 7 nm (2-h oxidation time), relative permittivity between 6.61 and 7.25, and leakage current density of $(1-7) \times 10^{-7}$ A/cm² at 2 MV/cm, and were successfully implemented into organic thin-film transistors based on pentacene and DNTT. The presence of –OH groups in all oxides is below the detection limit, while some carbon impurities appear to be incorporated.

© 2015 The Authors. Published by Elsevier B.V. This is an open access article under the CC BY license (<http://creativecommons.org/licenses/by/4.0/>).

1. Introduction

The ultra-thin and high-*k* dielectrics lead to field-effect transistors with low operating voltages. However, to achieve good transistor operation such dielectrics must also exhibit very low leakage current. HfLaO (*k* ~ 15.3) [1,2], Ba_{1.2}Ti_{0.8}O₃ (*k* ~ 15.57) [3], SrTiO₃ (*k* ~ 12.1) [4], and high-*k* polymers dielectrics (*k* ~ 12.6) [5] have been explored for low-voltage organic thin-film transistors (OTFTs). OTFTs with medium-*k* gate dielectrics such as aluminum oxide (*k* ~ 6.2) [6] have achieved low operating voltages through reduction in their thickness [7]. The aluminum oxide is often further functionalized by organic monolayers to provide reduction in the leakage current and the surface energy [8].

Standard deposition methods for aluminum oxide include sputtering and atomic layer deposition. However, ultra-thin layers of aluminum oxide can also be prepared by oxidation of aluminum deposited in high-vacuum by thermal evaporation [9,10],

sputtering, or e-beam. Oxidation of aluminum has been performed by low-frequency pulsed discharge plasma [11], oxygen plasma [10], or anodic oxidation [12]. For the growth of thicker oxide layers the oxygen plasma method is preferred, but such process leads to an increase in substrate temperature (~300 °C) that is not compatible with many plastic substrates.

The reactive atomic oxygen required for the oxidation of aluminum can also be produced by dissociation of ozone [13] and the oxidation can be performed at atmospheric pressure. UV/ozone oxidation was previously used in the preparation of high-*k* gate dielectrics for CMOS. Some examples include hafnium silicate [14], zirconia [15] and hafnium-aluminum oxynitride [13].

Prompted by our previous results achieved with UV/ozone oxidation of aluminum in the ambient air [16], this paper studies four different ozone oxidation methods that were applied to thermally evaporated aluminum layers. The produced oxide layers were implemented as gate dielectrics in OTFTs. Material characterization of the aluminum oxide (AlO_x) was correlated with the performance of organic transistors aiming to identify the best procedure for the AlO_x preparation.

The oxidation of aluminum was performed in UV/ozone cleaner system in ambient air, in which a high-pressure mercury lamp

* Corresponding author.

E-mail address: helena.gleskova@strath.ac.uk (H. Gleskova).

¹ Current address: Ecole Polytechnique Fédérale de Lausanne (EPFL), STI/IMT/IBI/LSBI, CH-1015 Lausanne, Switzerland.

emits UV light at 184.9 and 253.7 nm [16]. The higher energy photons are absorbed by the molecular oxygen, leading to ozone formation. The lower energy photons do not generate ozone. They illuminate the oxidizing surface, dissociate ozone, and assist in the removal of organic contaminants [17,18]. High-voltage discharge can also generate ozone [13]. Common commercial applications include water treatment and sanitation. Contrary to mercury lamps, the discharge produces ozone without the coexistence of high energy photons and the efficiency of the ozone generation depends on the relative humidity of the air. The results of this paper show for the first time that the ozone production method can have a profound effect on the properties of the produced AlO_x .

2. Experimental procedures

Four different methods of ozone generation have been implemented. The first one used UV/ozone cleaner (UVOCS) enclosed under a Hepa filter under ambient environmental conditions (21 °C, relative air humidity of ~45%). In the second case a flow of dry air (21 °C, relative air humidity $\leq 0.1\%$) was supplied into the UV/ozone cleaner, while the remaining parameters were kept the same. In the third case, dry air passed through high-voltage ozone generator (A2Z Ozone) and the generated ozone was supplied into the running UV/ozone cleaner (mercury lamp was on). Finally, the fourth method was similar to the third one, except the mercury lamp was turned off. This condition aimed to investigate the role of UV photons illuminating the aluminum layers during their oxidation. These four methods are summarized in Table 1.

All samples were prepared on Eagle 2000 glass substrates. Samples for spectroscopic ellipsometry, X-ray photoelectron spectroscopy (XPS) and Fourier Transform Infrared Spectroscopy (FTIR) started with ~30-nm-thick thermally evaporated Al layers. Samples were oxidized according to the conditions shown in Table 1 and the oxidation time was 2 h. The fifth sample was left to oxidize in dark ambient conditions to form a native oxide (Native AA). Finally, the UV-AA oxidation ranging from 5 min to 6 h was used to produce 6 samples. This allowed studying the thickness of the UV-AA AlO_x as a function of oxidation time.

Metal–insulator–metal (MIM) structures and organic thin-film transistors (OTFTs) were fabricated to study the effect of AlO_x oxidation process. Al/ AlO_x /DNTT/Au and Al/ AlO_x /C₈PA/pentacene/Au transistors were fabricated for four AlO_x oxidation procedures listed in Table 1 (DNTT stands for dinaphtho[2,3-b:2',3'-f]thieno[3,2-b]thiophene and C₈PA for n-octylphosphonic acid monolayer). The fabricated transistors have channel lengths of 30, 50, 70, and 90 μm and a channel width of 1000 μm . The corresponding MIM structures were fabricated alongside. Each sample contained 12 transistors and 4 MIM structures.

MIM structures were fabricated as follows. 30-nm-thick aluminum lines were deposited on glass substrate. One end of the lines was capped by gold layer to prevent their oxidation. AlO_x was prepared by using the four methods described above. In some samples, the AlO_x was functionalized with vapor-assembled monolayer of n-octylphosphonic acid (C₈PA) using the procedure

described in [19]. The presence of monolayer on top of aluminum oxide reduces the leakage current and changes the hydrophilic surface into hydrophobic [8]. The vacuum vapor growth of C₈PA monolayer was optimized with respect to the post-deposition annealing time [19,20], deposition temperature [21], and deposition rate [22]. All capacitors were completed by evaporating a 50-nm-thick gold layer [19]. The area of the capacitors was about 0.2 mm².

Bottom-gate, top-contact organic thin-film transistors (OTFTs) based on thermally evaporated DNTT (Sigma–Aldrich) or pentacene (Tokyo Chemical Industry) followed the same fabrication procedure. A 15-nm-thick DNTT was deposited directly on AlO_x , while a 50-nm-thick pentacene layer was deposited on AlO_x functionalized with C₈PA. Both transistor sets were completed by evaporating gold source and drain contacts. The cross-sections of pentacene and DNTT OTFTs are shown in Fig. 1. All fabrication steps were performed by using shadow masks. All thermal evaporation steps were conducted in Minispectros (Kurt J. Lesker) high vacuum system ($\sim 10^{-7}$ mBar) enclosed in a N₂-filled glove box.

The capacitor and transistor measurements were performed with Agilent B1500A semiconductor device analyzer under ambient environmental conditions. All fabricated devices were kept in oxygen and moisture-free environment until their measurement and they shared the same history. The gate dielectric capacitance of MIM structures was measured between 1 kHz and 1 MHz. The MIM current density was measured as a function of applied electric field. The transfer and output characteristics of the OTFTs were measured in a sweep mode. All fabricated MIM structures and transistors were measured for each AlO_x oxidation process. Mean values and standard deviations were calculated for all parameters.

The spectroscopic ellipsometry was performed with a J.A. Woollam M2000V in ambient air. Glass/Al/ AlO_x samples were measured and fitted with a three-layer model using a B-spline fit. FTIR was measured with Ge detector in reflection mode with Nicolet 380 spectrometer in ambient air. The beam diameter was ~1.5 mm. PeakFit analysis provided the location of the peaks, their intensity, full width at half maximum (FWHM), and integral area. Polycrystalline white corundum was also measured for comparison. X-ray photoelectron spectroscopy was carried out in a SAGE 100 system (Specs GmbH) using a non-monochromatic MgK α source, with a beam diameter of 7 mm, operated at 10 kV (150 W). The base pressure during the analysis was around 2×10^{-7} mBar. Spectra were recorded at a take-off angle of 90 degrees with a pass energy of the hemispheric analyser of 50 eV for survey scans and 15 eV

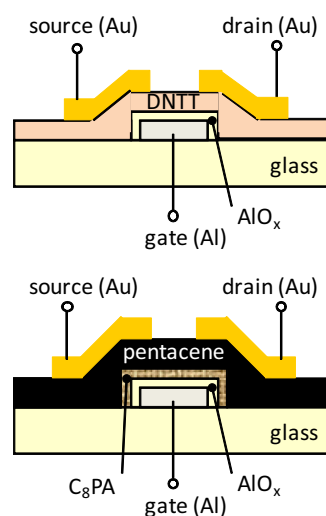


Fig. 1. OTFT cross-sections.

Table 1
Conditions of investigated aluminum oxidations. AA stands for ambient air and DA for dry air.

Procedure	Mercury lamp	Ozone flow	Air conditions	Relative humidity (%)
UV-AA	On	No	Ambient air	~45
UV-DA	On	No	Dry air	≤ 0.1
UV+O ₃ -DA	On	Yes	Dry air	≤ 0.1
O ₃ -DA	Off	Yes	Dry air	≤ 0.1

for detailed scans. Results were analyzed in commercial casaXPS software and composition was determined using peak fitting with a standard Shirley background. AlO_x/Al layers prepared in 4 different ways were examined. In addition, Al layer with native oxide and bulk sapphire material were measured for comparison. The sapphire was cleaned in situ with Ar plasma prior to the measurement while the AlO_x layers were not.

3. Results

3.1. Material characterization

Fig. 2a shows the AlO_x thickness obtained from the ellipsometry measurements. The UV/ozone oxidation in ambient air (UV-AA) resulted in AlO_x thickness of 7.06 ± 0.07 nm. The removal of the moisture from ambient air (UV-DA) led to a slightly thicker AlO_x layer of 7.15 ± 0.08 nm. The combination of mercury lamp and discharge-generated ozone (UV+O₃-DA) led to the highest thickness of 7.19 ± 0.09 nm. However, these three values are the same within the standard deviation. Finally, the discharge-generated ozone (O₃-DA) produced AlO_x of 6.85 ± 0.11 nm.

Fig. 2b depicts the measured capacitance of the AlO_x and $\text{AlO}_x/\text{C}_8\text{PA}$ MIM structures with AlO_x prepared using four different procedures. Going from UV-AA, to UV-DA and UV+O₃-DA, the AlO_x capacitance is gradually decreasing from ~ 0.90 to ~ 0.80 $\mu\text{F}/\text{cm}^2$

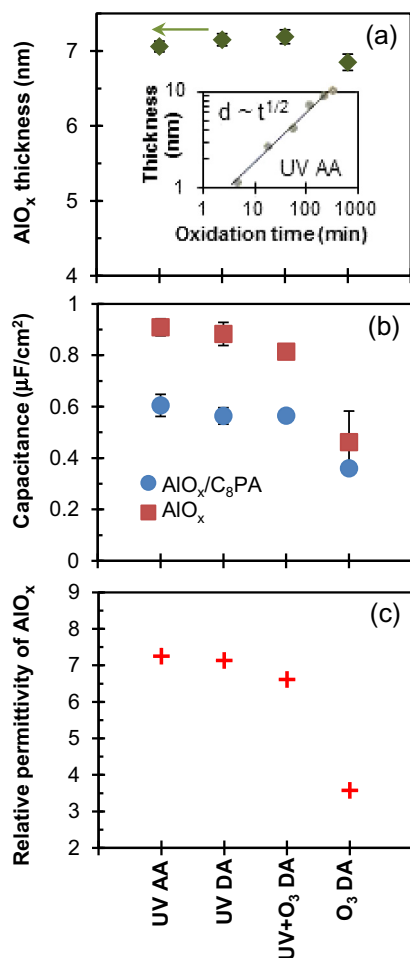


Fig. 2. AlO_x thickness (a), capacitance (b), and relative permittivity (c) as functions of the oxidation method. The inset in (a) depicts the thickness of AlO_x prepared by UV-AA method as a function of oxidation time. AA denotes ambient air, DA dry air, UV mercury lamp, and O₃ discharge-generated ozone.

cm^2 . However, the capacitance of the O₃-DA AlO_x layer is substantially lower, reaching only $0.46 \mu\text{F}/\text{cm}^2$. $\text{AlO}_x/\text{C}_8\text{PA}$ bi-layers prepared by discharge-generated ozone (O₃-DA) exhibit the lowest capacitance of $0.36 \mu\text{F}/\text{cm}^2$, while the remaining procedures led to a value of $\sim 0.60 \mu\text{F}/\text{cm}^2$. Finally, Fig. 2c shows the relative permittivity of AlO_x calculated from the known capacitance and thickness values. The relative permittivity decreased from 7.25 to 7.13 when the moisture was removed from the air. The addition of the discharge-generated ozone led to a further decrease in ϵ_r . However, the removal of the UV photons from the oxidation process resulted in a substantial reduction in ϵ_r to 3.58. Finally, the inset in Fig. 2a shows that the thickness of AlO_x prepared by UV/ozone oxidation in ambient air (UV-AA) follows approximately a square root dependence on the oxidation time with power exponent of 0.52.

Fig. 3 shows the leakage current density of AlO_x and $\text{AlO}_x/\text{C}_8\text{PA}$ MIM structures plotted as a function of applied electric field for different AlO_x oxidation procedures. The reduction in the air humidity from $\sim 45\%$ to $\leq 0.1\%$ led to a slight reduction in the AlO_x leakage current density when the UV lamp was used to produce the ozone (UV-AA versus UV-DA). Combination of the UV lamp and discharge-generated ozone (UV+O₃-DA) led to the lowest leakage current. If the UV lamp is not turned on and the ozone is produced via discharge (O₃-DA), the leakage current increases by several orders of magnitude. Qualitatively, the leakage current density is decreasing with increasing AlO_x thickness. However, the leakage current of UV-AA AlO_x is ~ 3 orders of magnitude lower than that of O₃-DA AlO_x , even though the difference in their thickness is only 3%.

When AlO_x is functionalized with C_8PA , the leakage current density is suppressed. With the exception of the discharge-generated ozone the leakage current density is $\sim 2\text{--}3 \times 10^{-7} \text{ A}/\text{cm}^2$ at the field of $-3 \text{ MV}/\text{cm}$. A visibly higher leakage current is observed for $\text{AlO}_x/\text{C}_8\text{PA}$ bi-layers with AlO_x produced with discharge-generated ozone (O₃-DA). Clearly, the presence of UV photons during the oxidation process is important for the leakage current reduction.

Fig. 4 shows XPS spectra for AlO_x layers prepared by different oxidation procedures. The spectrum of native oxide and bulk sapphire are also shown for comparison. Fig. 4b shows the section of XPS spectra corresponding to Al 2s and Al 2p peaks. With the exception of sapphire, all other Al 2s and Al 2p peaks exhibit a low energy 'shoulder', indicating presence of non-oxidized Al atoms.

Fig. 5a depicts the Al/O ratio obtained for AlO_x layers shown in Fig. 4. The ratio was calculated using the integrated intensities of the Al 2p and O 1s peaks and atomic sensitivity factors for Al and O. The ratio varied between ~ 1.1 and ~ 1.2 for various oxidation methods. The ratio measured for sapphire was 0.68, a value close

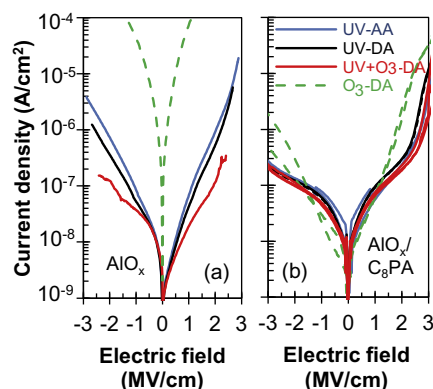


Fig. 3. Leakage current density of AlO_x (a) and $\text{AlO}_x/\text{C}_8\text{PA}$ (b) MIM structures as a function of applied electric field and AlO_x preparation method.

to the stoichiometric composition of Al_2O_3 . UV-AA and O_3 -DA AlO_x have similar Al/O ratio of ~ 1.15 . Other than the native AlO_x , UV-DA AlO_x exhibits the highest Al/O ratio of ~ 1.20 , while UV+ O_3 -DA AlO_x has Al/O ratio of ~ 1.10 . (These high Al/O values are reduced for AlO_x layers with thickness in excess of 8 nm, confirming that the electron escape depth is approximately 8 nm.) Fig. 5b depicts the ratio between the area of the lower-energy shoulder and the main peak for both Al 2s and Al 2p counts shown in Fig. 4b. The ratio for sapphire is zero, as all Al atoms are bonded to O. Since the low-energy peaks may be associated with the underlying Al, the smallest and largest ratio would be expected for UV+ O_3 -DA AlO_x (largest thickness of 7.19 nm) and the native oxide (1.67 nm), respectively. This is indeed observed experimentally. UV-AA AlO_x is only 3% thicker than O_3 -DA oxide. However, the discharge-generated ozone without the presence of UV photons resulted in a larger portion of unoxidized Al atoms.

Fig. 6a shows a section of the FTIR absorbance in the region between 700 and $\sim 1000\text{ cm}^{-1}$ that captures the stretching Al–O vibrations (bending vibrations are located below 500 cm^{-1} [23]). Polycrystalline white corundum shows a broad peak that reaches maximum at 730 cm^{-1} and a weaker absorption centered near 793 cm^{-1} . In addition, minute absorption is also located near 770 and 899 cm^{-1} . The Al–O absorbance of AlO_x layers prepared using ozone oxidation techniques is shifted to higher wavenumbers. A small peak is observed at 731 cm^{-1} coinciding with the absorbance in corundum. The large broad bands are a superposition of three main absorbances located at ~ 850 , ~ 900 and $\sim 950\text{ cm}^{-1}$. However, their amplitude and relative contribution to the absorption band are changing with the oxidation method. The absorbance reaches maximum at $\sim 930\text{ cm}^{-1}$ for UV-AA, UV-DA and UV+ O_3 -DA oxides. On the contrary, the absorbance peaks are similar for O_3 -DA and native oxides. They reach maximum at lower wavenumbers due to the highest amplitude at 850 cm^{-1} . The shape of the absorbance is somewhat correlated with the relative permittivity of AlO_x ; higher ϵ_r results in the higher contribution of the high-wavenumber absorbance.

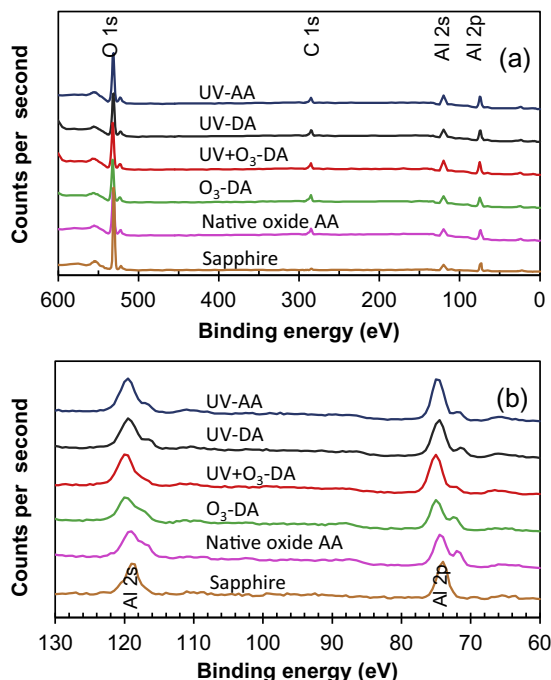


Fig. 4. XPS spectra (a) and Al 2s and Al 2p peaks (b) for AlO_x layers of Fig. 2. Native oxide and bulk sapphire are shown for comparison.

The assignment of the absorbance peaks of ozone oxidized layers is difficult. It is well known that compounds which contain AlO_4 -tetrahedra in their structure exhibit an absorption band at higher wavenumbers than materials consisting of AlO_6 -octahedra. In addition, the disorder in amorphous films leads to a distribution in the oscillator strengths and frequencies of Al–O stretching modes, resulting in broad absorbance peaks. The Al–O bond length also affects the position of the Al–O band; the absorbance at higher wavenumber results from shorter Al–O bonds [24]. For example, the subsurface oxygen exhibits a stretching mode between 820 and 875 cm^{-1} [25]. The Al–O–H deformation mode is also present near 850 cm^{-1} . This mode was observed at 840 cm^{-1} for the condensation reaction of octadecylphosphonic acid onto aluminum oxide/hydroxide surface [26] and measured near 840 – 847 cm^{-1} in kaolinites [27]. However, the associated Al–O–H stretching modes are expected between 3200 and 3700 cm^{-1} [28] where they overlap with the H–O–H stretching mode of water. The AlO_x layers of Fig. 6 do not show measurable absorbance above 3000 cm^{-1} . Consequently, the absorbance near 850 cm^{-1} is associated with the presence of subsurface oxygen instead of –OH groups, indicating that the UV light promotes oxygen diffusion from the surface inward.

Not counting the native AlO_x , the largest integral intensity is measured for UV-AA oxide and the lowest for O_3 -DA AlO_x , even though their thicknesses are comparable (see Fig. 2a). The use of dry air (UV-DA, UV+ O_3 -DA and O_3 -DA) produced lower integral absorbance than the ambient air. Overall, the integral absorbance is not correlated with the AlO_x thickness. Since the reflectivity of Al in the region between 2.5 and $25\text{ }\mu\text{m}$ is $>98\%$, the contribution from the underlying Al and glass to the IR absorbance can be neglected.

Fig. 6b shows the region of symmetric and antisymmetric stretching vibrations of methyl and methylene groups. Fig. 4a shows the presence of C 1s peaks for all AlO_x layers regardless of their preparation and the FTIR measurements suggest that some of this carbon is incorporated in the AlO_x layers. UV-AA and O_3 -DA AlO_x exhibit the highest peak amplitudes, followed by slightly lower absorbance from UV+ O_3 -DA, and the lowest absorbance from UV-DA and native AlO_x . The insignificant absorbance measured for corundum is ascribed to ambient methane. Qualitatively similar behavior with respect to peak amplitudes is observed in the region from ~ 1300 to $\sim 1500\text{ cm}^{-1}$ (rocking, wagging, and bending modes of $-\text{CH}_2$ and $-\text{CH}_3$).

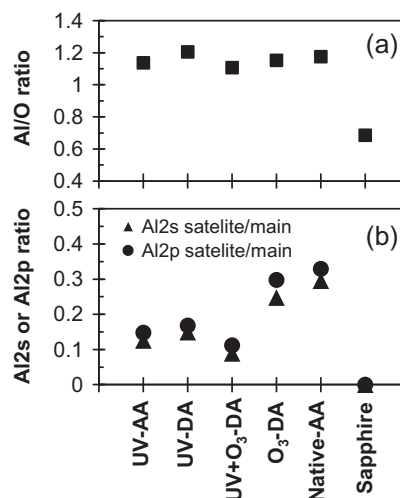


Fig. 5. Al/O ratio (a) and Al 2s and Al 2p peak-ratios (b) for AlO_x layers of Fig. 4.

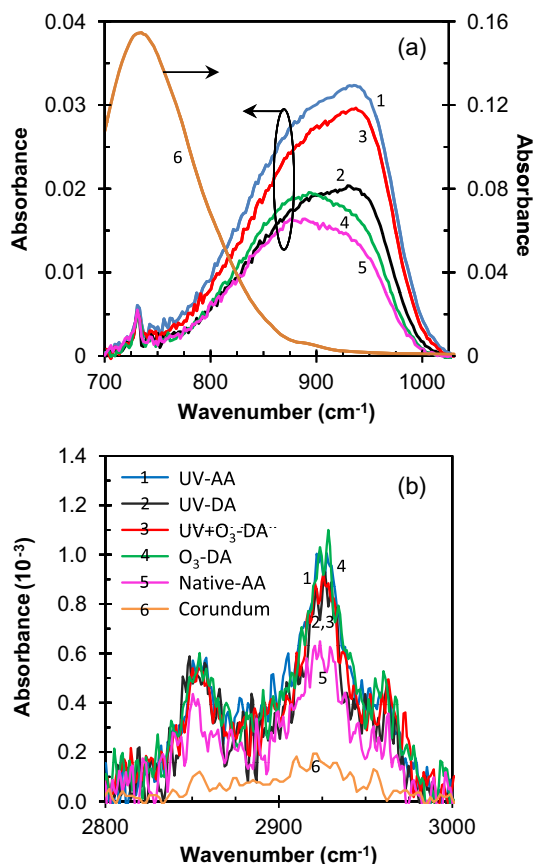


Fig. 6. FTIR spectra of AlO_x prepared using different oxidation methods. Polycrystalline white corundum is shown as a reference.

3.2. OTFT properties

In this section, OTFT properties are presented for all oxidation methods other than O_3 -DA due to the excessive leakage current density produced with this method. The transfer and output characteristics of $\text{Al}/\text{AlO}_x/\text{C}_8\text{PA}/\text{pentacene}/\text{Au}$ transistor with $L = 24 \mu\text{m}$ and $W = 1000 \mu\text{m}$ are shown in Fig. 7. The threshold voltage and field-effect mobility of $\text{Al}/\text{AlO}_x/\text{DNTT}/\text{Au}$ transistors are shown in Fig. 8a and b. Although the functionalization of AlO_x with phosphonic acid is preferred for DNTT transistors, the transistor parameters are affected by the quality of AlO_x and its interface with DNTT and thus provide valuable information [29]. The threshold voltage is $\sim -1.15 \text{ V}$ for the UV-AA and UV-DA oxidations and $\sim -1.25 \text{ V}$ for UV+ O_3 -DA AlO_x . The field-effect mobility is $0.0014 \text{ cm}^2/\text{Vs}$ for UV-AA, $0.017 \text{ cm}^2/\text{Vs}$ for UV-DA and $0.0007 \text{ cm}^2/\text{Vs}$ for UV+ O_3 -DA oxidations. The threshold voltage and field-effect mobility of $\text{Al}/\text{AlO}_x/\text{C}_8\text{PA}/\text{pentacene}/\text{Au}$ transistors are shown in Fig. 8c and d. The threshold voltage is $\sim -1.5 \text{ V}$ for the UV-DA and UV+ O_3 -DA oxidations and $\sim -1.3 \text{ V}$ for UV-AA AlO_x . The field-effect mobility is $\sim 0.055 \text{ cm}^2/\text{Vs}$ for UV-AA and UV+ O_3 -DA oxidations and $\sim 0.045 \text{ cm}^2/\text{Vs}$ for OTFTs with UV-DA AlO_x .

4. Discussion

UV-AA and UV-DA oxides are both prepared under UV lamp using different level of moisture in the ambient air. The reduction from ~ 45 to $<0.1 \text{ RH\%}$ led to an increase in the oxide thickness from 7.06 to $\sim 7.15 \text{ nm}$, a decrease in ϵ_r from 7.25 to 7.13 , a factor of two reduction in the leakage current density, a slight increase in the Al/O ratio and the fraction of unoxidized Al, and reduction in

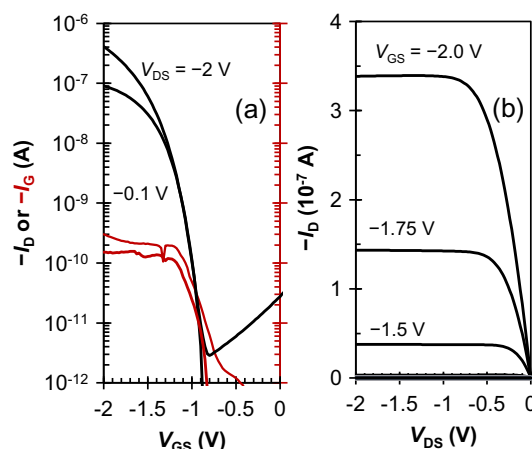


Fig. 7. Transfer (a) and output (b) characteristics of $\text{Al}/\text{AlO}_x/\text{C}_8\text{PA}/\text{pentacene}/\text{Au}$ transistor with $L = 24 \mu\text{m}$ and $W = 1000 \mu\text{m}$.

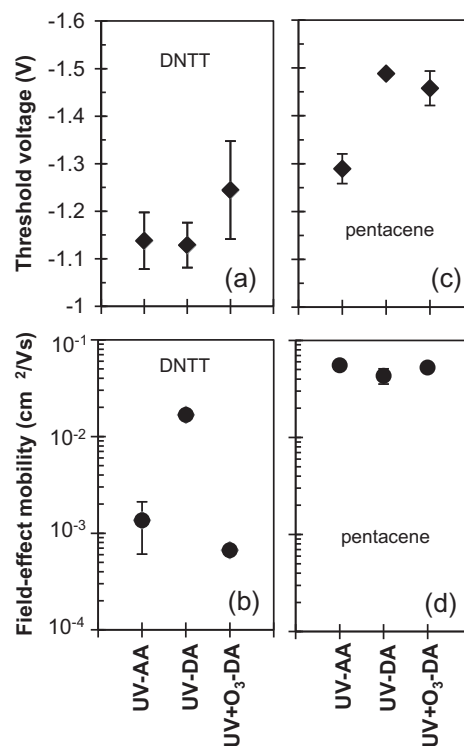


Fig. 8. Threshold voltage (a and c) and field-effect mobility (b and d) of $\text{Al}/\text{AlO}_x/\text{DNTT}/\text{Au}$ (a and b) and $\text{Al}/\text{AlO}_x/\text{C}_8\text{PA}/\text{pentacene}/\text{Au}$ (c and d) OTFTs as function of the AlO_x preparation. For the mobility variation smaller than $\sim \pm 10\%$ the standard deviations are not visible.

$\text{Al}-\text{O}$ absorbance and absorbance associated with C impurities. These results confirm that dry air oxidation results in lower oxygen and carbon content in the formed AlO_x layer.

At the same time, the threshold voltage of the DNTT transistors was similar, while the $|V_t|$ of pentacene transistors was increased by $\sim 0.2 \text{ V}$. The field-effect mobility increased by an order of magnitude for DNTT transistors and reduced by $\sim 20\%$ for pentacene transistors. Since the growth of both pentacene [30] and DNTT [31] depends on the surface energy of the underlying surface, the change in the field-effect mobility of DNTT OTFTs suggests change in the AlO_x surface chemistry between ambient and dry air oxidations. After the AlO_x surface is modified with C_8PA monolayer, C_8PA

surface properties control the pentacene growth, resulting in similar OTFT field-effect mobilities.

Comparison of UV-DA and UV+O₃-DA oxides reveals the effect of the added ozone produced via high-voltage discharge. The addition of the discharge-generated ozone leads to a marginal increase in the oxide thickness, slight decrease in its ϵ_r , a factor of two reduction in the leakage current density, decreased Al/O ratio and the fraction of unoxidized Al, increased Al–O absorbance and similar absorbance associated with C impurities. An increase in $|V_t|$ of DNTT transistors by ~ 0.1 V and a slight reduction in $|V_t|$ for pentacene transistors were observed. The field-effect mobility was reduced by a factor of ~ 25 for DNTT transistors and increased by $\sim 20\%$ for pentacene transistors. Overall, the addition of ozone produced via high-voltage discharge did not improve the properties of AlO_x layer, even though there was a slight improvement in the leakage current density and the fraction of unoxidized Al. The transistor parameters are also inferior when compared to UV-AA oxides.

UV-AA and O₃-DA oxides have comparable thickness and Al/O ratio. However, UV-AA oxidation leads to much higher ϵ_r and much lower fraction of unoxidized Al. In addition, their Al–O absorbance is also different. UV-AA AlO_x exhibits larger integral area with stronger absorbance near 950 cm^{−1}, while O₃-DA AlO_x shows smaller area with dominating absorbance near 850 cm^{−1} characteristic of subsurface oxygen. At the same time the absorbance due to presence of carbon is similar in both oxides. One can infer from this that while both oxides contain comparable amount of oxygen, the presence of high-energy photons during UV-AA oxidation facilitates the diffusion of the O atoms and their insertion into the Al network, resulting in stronger Al–O vibration peak, factor of two higher ϵ_r , and a factor of ~ 500 smaller leakage current density.

The threshold voltage is also affected by the oxidation of aluminum. The lowest threshold voltage was achieved for UV-AA oxidized AlO_x for both DNTT and pentacene transistors. Finally, all OTFTs exhibit field-effect mobility lower than that reported by others [29,32,33] and further optimization is required to increase the mobility of DNTT OTFTs.

5. Conclusions

Thin aluminum oxide films were prepared by exposing Al layers to ozone generated by UV lamp and/or high-voltage discharge. Four oxidation methods have been tested, namely the UV/ozone oxidation in ambient (UV-AA) and dry (UV-DA) air, UV/ozone oxidation combined with discharge-generated ozone in dry air (UV+O₃-DA), and discharge-generated ozone in dry air (O₃-DA). The AlO_x layers were evaluated with spectroscopic ellipsometry, X-ray photoelectron spectroscopy and Fourier transform infrared spectroscopy. The capacitance and leakage current density of Al/AlO_x/Au and Al/AlO_x/C₈PA/Au metal–insulator–metal structures were also measured and the relative permittivity of AlO_x was extracted. Finally, the thin-film transistors based on pentacene and DNTT were fabricated to evaluate the suitability of the atmospheric pressure oxidation methods for organic electronics.

The lack of the high-energy photons during O₃-DA oxidation led to a low relative permittivity and high leakage current density of the AlO_x layer that rendered this method unsuitable for transistor dielectrics. Although the oxygen was incorporated into the film, the FTIR confirmed an increased concentration of subsurface oxygen while the XPS gave the highest portion of the unoxidized Al among all four methods. Overall, the presence of UV photons

during the oxidation process promotes the diffusion of the oxygen and its incorporation into the AlO_x lattice.

The AlO_x layers prepared using UV lamp (UV-AA, UV-DA, UV+O₃-DA) produced device quality oxides. Although there are minor differences in their properties, the 2-h oxidation produced AlO_x films with thickness in excess of 7 nm, relative permittivity between 6.61 and 7.25, and leakage current density of $(1\text{--}7) \times 10^{-7}$ A/cm² at 2 MV/cm. All oxides contain some carbon impurities while the presence of –OH groups is below the detection limit.

Acknowledgments

The authors thank D.M. Taylor from Bangor University for providing access to spectroscopic ellipsometer. This research was supported by the Scottish Funding Council through Glasgow Research Partnership in Engineering. Stuart Hannah acknowledges support from the EPSRC. FTIR results were partially developed within the CENTEM project, Reg. No. CZ.1.05/2.1.00/03.0088 co-funded by the ERDF within the OP RDI programme, and in the follow-up sustainability stage, supported through CENTEM+ (LO1402) by the Ministry of Education, Youth and Sports of the Czech Republic under the National Sustainability Programme I.

References

- [1] M.F. Chang, P.T. Lee, S.P. McAlister, A. Chin, *IEEE Electron Device Lett.* 30 (2009) 133.
- [2] L.F. Deng, P.T. Lai, W.B. Chen, J.P. Xu, Y.R. Liu, H.W. Choi, C.M. Che, *IEEE Electron Device Lett.* 32 (2011) 93.
- [3] C.-Y. Wei, S.-H. Kuo, Y.-M. Hung, W.-C. Huang, F. Adriyanto, Y.-H. Wang, *IEEE Electron Device Lett.* 32 (2011) 90.
- [4] H. Yan, H. Hanagata, T. Jo, H. Okuzaki, *Jpn. J. Appl. Phys.* 50 (2011) 01BC05.
- [5] S.H. Kim, S.Y. Yang, K. Shin, H. Jeon, J.W. Lee, K.P. Hong, C.E. Park, *Appl. Phys. Lett.* 89 (2006) 183516.
- [6] J. Lee, J.H. Kim, S. Im, *J. Appl. Phys.* 95 (2004) 3733.
- [7] K.D. Kim, C.K. Song, *Appl. Phys. Lett.* 88 (2006) 233508.
- [8] H. Klauk, U. Zschieschang, J. Pfau, M. Halik, *Nature* 445 (2007) 745.
- [9] S. Ge, J.J. Chen, N.A. Bojarczuk, H. Shang, M. Copel, J.B. Hannon, J. Karasinski, E. Preisler, S.K. Banerjee, S. Guha, *IEEE Trans. Electron Device* 51 (2004) 1441.
- [10] A. Quade, H. Wulff, H. Steffen, T.M. Tun, R. Hippler, *Thin Solid Films* 377 (2000) 626.
- [11] Y. Li, L. Wang, *Thin Solid Films* 517 (2009) 3208.
- [12] M. Kaltenbrunner, T. Sekitani, J. Reeder, T. Yokota, K. Kuribara, T. Tokuhara, M. Drack, R. Schwödlauer, I. Graz, S. Bauer-Gogonea, S. Bauer, T. Someya, *Nature* 499 (2013) 458.
- [13] Y.-Y. Chen, *Microelectron. Eng.* 87 (2010) 62.
- [14] P. Punchaipetch, G. Pant, M.A. Quevedo-Lopez, C. Yao, M. El-Bouanani, M.J. Kim, R.M. Wallace, B.E. Gnade, *IEEE J. Select. Top. Quantum Electron.* 10 (2004) 89.
- [15] S. Ramanathan, P.C. McIntyre, *Appl. Phys. Lett.* 80 (2002) 3793.
- [16] K.C. Chinnam, S. Gupta, H. Gleskova, J. Non-Cryst. Solids 358 (2012) 2512.
- [17] J.R. Vig, *J. Vac. Sci. Technol. A* 3 (1985) 1027.
- [18] J.R. Vig, J.W. Le Bus, *IEEE Trans. Parts Hybrids Package PHP-12* (1976) 365.
- [19] S. Gupta, H. Gleskova, *Org. Electron.* 14 (2013) 354.
- [20] H. Gleskova, S. Gupta, P. Šutta, *Org. Electron.* 14 (2013) 3000.
- [21] S. Gupta, P. Šutta, D.A. Lamprou, H. Gleskova, *Org. Electron.* 14 (2013) 2468.
- [22] S. Gupta, H. Gleskova, *Euro Display Proc.* 44 (2013) 135.
- [23] W.W. Peng, P. Roy, L. Favaro, E. Amzallag, J.B. Brubach, A. Congeduti, M.A. Guidi-Cestelli, A.M. Huntz, J. Barros, R. Tétot, *Acta Mater.* 59 (2011) 2723.
- [24] G. Santambrogio, E. Janssens, S. Li, T. Siebert, G. Meijer, K.R. Asmis, J. Döbler, M. Sierka, J. Sauer, *J. Am. Chem. Soc.* 130 (2008) 15143.
- [25] V.M. Bermudez, R.L. Rubinovitz, J.E. Butler, *J. Vac. Sci. Technol. A* 6 (1988) 717.
- [26] P. Thissen, A. Vega, T. Peixoto, Y.J. Chabal, *Langmuir* 28 (2012) 17494.
- [27] B.J. Saikia, G. Parthasarathy, *J. Mod. Phys.* 1 (2010) 206.
- [28] E. Balan, M. Lazzeri, G. Morin, F. Mauri, *Am. Miner.* 91 (2006) 115.
- [29] S. Bisoyi, U. Zschieschang, M.J. Kang, K. Takimiya, H. Klauk, S.P. Tiwari, *Org. Electron.* 15 (2014) 3173.
- [30] K. Fukuda, T. Hamamoto, T. Yokota, T. Sekitani, U. Zschieschang, H. Klauk, T. Someya, *Appl. Phys. Lett.* 95 (2009) 203301.
- [31] T. Yamamoto, K. Takimiya, J. Photopolym. Sci. Technol. 20 (2007) 57.
- [32] U. Zschieschang, R. Hofmockel, R. Rödel, U. Kraft, M.J. Kang, K. Takimiya, T. Zaki, F. Letzkus, J. Butschke, H. Richter, J.M. Burghartz, H. Klauk, *Org. Electron.* 14 (2013) 1516.
- [33] K. Fukuda, T. Yokota, K. Kuribara, T. Sekitani, U. Zschieschang, H. Klauk, T. Someya, *Appl. Phys. Lett.* 96 (2010) 053302.